



Novel optical technologies for emergency preparedness and response: Mapping contaminations with alpha-emitting radionuclides

Maksym Luchkov^a, Volker Dangendorf^a, Ulrich Giesen^a, Frank Langner^a, Claudia Olaru^b, Mastaneh Zadehrafai^b, Annika Klose^c, Kim Kalmankoski^d, Johan Sand^e, Sakari Ihantola^e, Harri Toivonen^e, Clemens Walther^c, Stefan Röttger^a, Mihail-Razvan Ioan^b, Juha Toivonen^d, Faton S. Krasniqi^{a,*}

^a *Physikalisch-Technische Bundesanstalt (PTB), Bundesallee 100, 38116 Braunschweig, Germany*

^b *“Horia Hulubei” National Institute for R&D in Physics and Nuclear Engineering (IFIN-HH), Reactorului no.30, P.O.BOX MG-6, Bucharest - Magurele, Romania*

^c *Gottfried Wilhelm Leibniz Universität Hannover, Institut für Radioökologie und Strahlenschutz (IRS), Herrenhäuser Str. 2, 30419, Hannover, Germany*

^d *Photonics Laboratory, Physics Unit, Tampere University, 33101 Tampere, Finland*

^e *Alfa Rift Ltd, Insinöörinkatu 54, 33720 Tampere, Finland*

ARTICLE INFO

Keywords:

Radioluminescence
Optical detection of alpha emitters
Emergency preparedness
Lens-based detection systems
UV-A
UV-C

ABSTRACT

Radiological emergencies involving an accidental or deliberate dispersion of alpha-emitting radionuclides in the environment can cause significant damage to humans and societies in general. Currently, there is a metrology gap in managing such emergencies due to the lack of detectors that can measure alpha particles at distances greater than their range in air: most conventional alpha detectors are only effective when placed just a few centimeters above the contaminated area. This paper presents the development and testing of lens based optical detection systems that utilize alpha particle-induced ultraviolet (UV) luminescence of air, known as alpha radioluminescence. Telescopes based on fused silica and Poly(methyl 2-methylpropenoate) (PMMA) Fresnel lenses were investigated for their usability in facilitating emergency management related to alpha-emitting radionuclides. Careful matching of the diameter and focal length of the receiving optics, the response of the photocathode, and the passband of the filter allows detection sensitivities as high as $34 \text{ s}^{-1} \text{ MBq}^{-1}$ at 2 m source-to-detector distance and background count rate of about 3 s^{-1} in the UV-C spectral region, and suppression of daylight background count rate down to 16 s^{-1} . By flushing the source with nitrogen (N_2) containing trace amounts of nitric oxide (NO), a groundbreaking sensitivity of $1.3 \times 10^5 \text{ s}^{-1} \text{ MBq}^{-1}$ has been achieved, allowing detection limits as low as 100 Bq with room lighting on, and 70 Bq in a dark environment. In the UV-A spectral region, a detection limit of 4 kBq could be achieved in a dark environment. These optical detection systems are aimed to facilitate a rapid, coordinated, and effective response in emergency situations involving the release of alpha-emitting radionuclides by mounting them on a tripod or an unmanned aerial device (UAV).

1. Introduction

Alpha-emitting radionuclides can cause severe damage to sensitive living tissue when inhaled, swallowed or when incorporated through open wounds. The amount of energy they release in the human body is up to 6 million times greater than that of an ordinary chemical reaction (ordinary chemical energy used by cells in the body), which means that a single alpha particle has the ability to severely or lethally damage all the cells within its range [1]. Therefore, the release of alpha-emitting radionuclides in the environment, such as by nuclear terroristic attacks or transportation accidents, as well as by severe emergencies in nuclear installations, represent a major radiological threat to human beings if they enter the human body.

In the case of a large-scale nuclear or radiological emergency involving accidental or deliberate dispersion of alpha-emitting radionuclides into the environment, depending on their distribution pattern and meteorological conditions such as wind and precipitation, large areas could be contaminated. The dust and debris in such events would be highly radioactive and can potentially be inhaled, thus posing a serious threat to the exposed population. In this case, detection of alpha-emitting radionuclides with traditional detectors is inherently uncertain due to low spatial resolution, and time consuming and tedious due to their short range (e.g., about 42 mm for a 5.5 MeV particle) [2]. This approach involves scanning near contaminated surfaces, exposing the personnel to other hazards and risks such as other types of radiation,

* Corresponding author.

E-mail address: faton.krasniqi@ptb.de (F.S. Krasniqi).

fire, etc. [3]. Therefore, new detection techniques which keep both the operator and the detector at safe distance from the contaminated area are needed.

Recently, the detection of alpha particle-emitting sources by optical means has gained increasing interest. In this approach, alpha particles are detected indirectly by utilizing physical effects such as alpha particle-induced luminescence (radioluminescence) [3–15], laser probing of alpha induced excited state of air molecules, and laser probing of collisional ionization (breakdown) of the air [16–19]. While laser-based methods are still emerging, radioluminescence technology is already mature and its feasibility has been demonstrated in many experiments [3–15]. Radioluminescence in air is generated mostly by emission of molecular nitrogen (N_2), and to a much lesser extent, by trace amounts of nitric oxide (NO) in air, with wavelength spanning three ultraviolet bands and about 99% of emission occurring in the 280 nm to 440 nm spectral range [4,5]. There are, however, significant challenges for remote optical detection of alpha-emitting radionuclides, since the spectrum of radioluminescence overlaps with that of solar radiation and is obscured by it at wavelengths longer than 280 nm due to much stronger solar irradiance [3–5,13]. At wavelengths shorter than 280 nm, on the other hand, the background light is very weak, in particular with daylight, because most of solar radiation is absorbed by the atmospheric ozone [8–12,14,15]; The intensity of UV-C radioluminescence with wavelengths between 200 nm and 280 nm, however, is very low (<1%). Thus, both cases impose strict limitation on the wide application of this technique. A major breakthrough that opened the opportunity for overcoming the above-mentioned fundamental limitations was reported by Kerst et al. [9] who showed that adding trace amounts of nitric oxide to the nitrogen atmosphere surrounding the sample drastically increases the radioluminescence signal, with almost all of the emission located in the UV-C spectral region.

Successful detection of weak spectral fingerprints due to the alpha radioluminescence in the environment is a challenging task that goes beyond the current state-of-the-art measurement techniques applied for contamination detection and emergency management. In this work, the performance and usability of three field capable lens-based optical detection systems have been evaluated. These systems have been developed in the framework of the European Metrology Program for Innovation and Research (EMPIR) project RemoteALPHA [20], which aims to develop novel instruments and methods as well as a sustainable metrological infrastructure for the optical detection of alpha-emitting radionuclides in the environment. One detection system is based on a high-quality UV fused silica (UVFS) lens while the other two use PMMA Fresnel lenses. Compared to previously used instruments [4–15], these systems were designed from their inception to facilitate emergency management by maximizing radioluminescence throughput using large receiving optics and keeping the background signal low through efficient wavelength filtering and low noise photomultipliers (PMT). All systems can be operated as scanning telescopes, with the Fresnel lens systems also being suitable to be used in UAVs as unmanned aerial monitoring systems (UAMS). The detection efficiency of all systems has been measured at the PTB Ion Accelerator Facility (PIAF) where alpha particles with a rate from $5 \times 10^4 \text{ s}^{-1}$ to about $4.5 \times 10^7 \text{ s}^{-1}$, collimated to a beam size of $100 \mu\text{m} \times 100 \mu\text{m}$, have been accelerated to energies up to 8.3 MeV. In the context of radioluminescence detection of alpha particles, such a finely collimated beam acts like a point alpha source (see Section 4). Therefore, the sensitivity of optical detection setups is expressed in $\text{s}^{-1} \text{MBq}^{-1}$ (alias cps/MBq) and the detection limit in Bq instead of s^{-1} . The relationship between radioluminescence photons and alpha activity is calibrated with a dedicated ^{210}Po activity standard [21].

The radioluminescence mapping capability is demonstrated with the UVFS telescope which has been used to obtain the radioluminescence image of (a) deceleration of alpha particles at the exit port of the PIAF microbeam, (b) dedicated Am-241 sample designed to simulate an extended alpha source, and (c) low activity pitchblende minerals with surface activity between 80 Bq cm^{-2} and 105 Bq cm^{-2} .

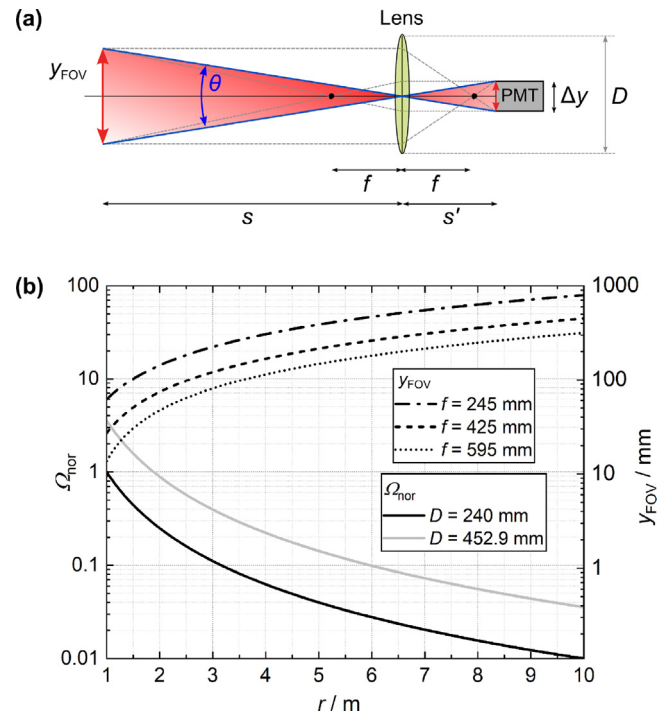


Fig. 1. (a) Schematic illustration of the field-of-view (FOV) in a radioluminescence detection setup composed of a lens and a photomultiplier (PMT). The focal length of a lens is denoted by f while θ is the angle of view. The FOV at the object distance s is $y_{\text{FOV}} = \Delta y (s/s')$, with Δy being the size of the detector sensitive area (diameter of the PMT photocathode), s and s' the object and image distance. (b) Geometrical factor $\Omega_{\text{nor}} = \pi D^2 / (4 r^2)$ with D being the diameter of the receiving optics and r the distance between source and receiving optics, normalized to the value for $D = 240 \text{ mm}$ and $r = 1 \text{ m}$. The right side plots the field of view y_{FOV} with $s = r$ and $\Delta y = 20 \text{ mm}$.

2. Description of optical detection systems

The successful detection of spectral fingerprints due to alpha radioluminescence in the environment requires optical systems which efficiently detect light in the characteristic wavelengths of radioluminescence photons, but at the same time stay as insensitive as possible to the ambient light. A high radioluminescence light throughput for the optical detection system requires a compromise between the diameter of the receiving optics, D , and the focal length of the system, f , because the overall efficiency of the detection system depends on the f-number $N = f/D$. The diameter of the receiving optics determines the so-called geometrical efficiency, which represents the solid angle subtended by the receiving optics and thus directly affects the number of photons entering the detection system. The focal length, on the other hand, determines the angle of view, which in turn affects both the number of detected photons and filtering [see Fig. 1(a)]. Interference filters should transmit only the selected radioluminescence band. Since the transmission band of these filters is subject to a blue shift at non-normal light incidence, optics with a long focal length are required to ensure a narrow angular distribution of the radioluminescence light on the filter without the need for additional optical elements which would cause additional light losses. When considering the contaminated area as an ensemble of point sources, the f-number must be chosen to maximize geometric efficiency while maintaining an acceptable field of view that does not significantly blur the scanned radioluminescence image. To illustrate this point, geometrical efficiency and field-of-view (FOV) are plotted as a function of source-to-detector distance in Fig. 1(b). While the light collection efficiency scales with r^{-2} , with r being the source-to-detector distance, the FOV is proportional to r .

The lens-based optical detection prototypes developed as part of the RemoteALPHA project were designed to comply with the requirements

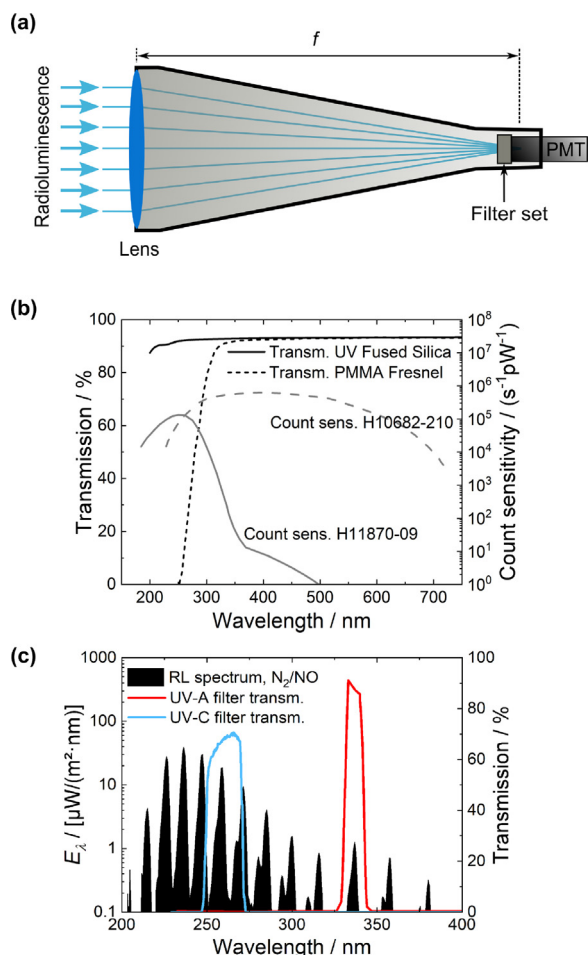


Fig. 2. (a) Schematic drawing of optical systems developed in the framework of RemoteALPHA project. Both, the UVFS- and PMMA Fresnel-lens systems share the same configuration: they utilize large receiving optics to maximize the geometrical factor, and the focal lengths have been chosen such that the radioluminescence image is not blurred substantially by the overlapping FOVs between adjacent scanning points. (b) Transmittance spectra of UVFS [22] and PMMA [23] together with the PMT count sensitivity [24,25] specified by the manufacturer. (c) Radioluminescence emission spectrum of NO measured at the PIAF at a nominal alpha particle rate of about $30 \times 10^6 \text{ s}^{-1}$ with a PTB-calibrated array spectroradiometer with UV-C and UV-A filter transmission [26,27]. The flow rate of $\text{N}_2 + \text{NO}$ was set at 2400 mL min^{-1} with NO concentration of $5 \mu\text{L L}^{-1}$.

stated above. They share the same configuration, see Fig. 2(a): an objective lens (UVFS with a diameter of 240 mm or a PMMA Fresnel lens with diameters of 452.9 mm or 257.6 mm), a filter set to select the operating wavelength range (UV-A or UV-C) and a PMT with a cathode material (bialkali or cesium telluride) according to the wavelength range selected by the filter set. The transmittance spectra of the lenses, together with the count sensitivities of the used PMTs, are shown in Fig. 2(b). The measured radioluminescence spectra with UV-C and UV-A filter absorption curves are shown in Fig. 2(c).

All three systems operate as mapping systems by producing the radioluminescence image of the alpha-emitting sources through remote scanning of narrow FOV over the user-defined region of interest while recording the photon count rate. In contrast to imaging mode which requires additional optical elements to correct image distortions and aberrations, these configurations are designed for a minimum number of refractive elements in order to reduce unnecessary light losses. Moreover, since image formation is not necessarily required, more than one interference filters can be used without considering distortions that arise from multiple reflective surfaces. While the UVFS system, due to constraints related to its weight and mechanical stability, is

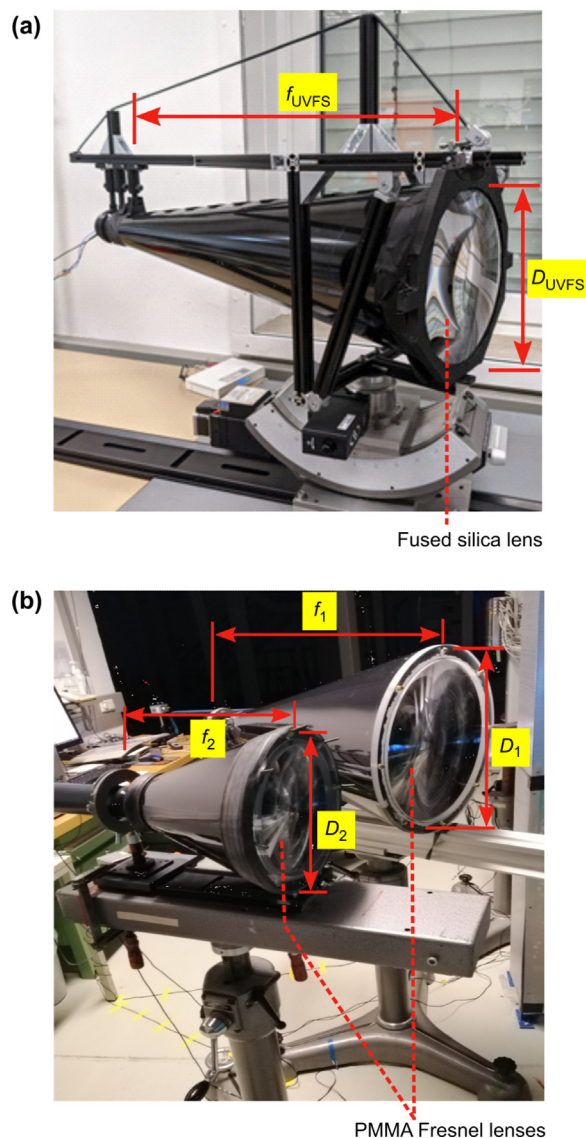


Fig. 3. Lens-based radioluminescence detection setups. (a) Fused silica lens (Abet Technologies) system mounted on a goniometer and rotation stage (Newport M-BGM160PE and RV80CC) with $D_{UVFS} = 240 \text{ mm}$ and f_{UVFS} between 572 mm to 599 mm in a wavelength range from 236 nm to 285 nm, respectively. (b) PMMA Fresnel lens systems with lenses (Orafol Fresnel Optics) having diameters $D_1 = 452.9 \text{ mm}$ (SC 2045) and $D_2 = 257.6 \text{ mm}$ (SC 210), and nominal focal lengths $f_1 = 391.5 \text{ mm}$ and $f_2 = 225.5 \text{ mm}$ at 546 nm. All lens systems can be coupled to Hamamatsu PMTs (H10682-210 for UV-A spectral range and H11870-09 for UV-C spectral range) and UV-C filters (FF01-260/16-25, Semrock Inc.) or UV-A filters (337 nm, 10 nm band-pass filters from Edmund Optics).

being anticipated for use as a scanning telescope mounted on a tripod, the lens systems based on the Fresnel lenses—being lightweight (less than 5 kg)—will be optimized in the framework of RemoteALPHA as an unmanned airborne monitoring system for mapping of alpha contaminations in the environment. Fig. 3 shows the three lens-based optical systems developed within RemoteALPHA. By using the appropriate interference filters and PMTs, they can operate both in UV-A and UV-C spectral region. While the Fresnel lens systems exploit the full advantage of their large diameters in the UV-A region, their use in the UV-C spectral region is less efficient due to the transmission cutoff at 260 nm, see Fig. 2(b). The fused silica lens, on the other hand, has high transmission in both the UV-A and UV-C spectral regions.

3. Experimental setup

The performance of the developed radioluminescence detection systems has been tested at the microbeam facility of the PIAF [28]. Here, a compact cyclotron and microbeam system was used to provide a narrowly focused alpha beam with a size of about $100\ \mu\text{m} \times 100\ \mu\text{m}$ at the entrance of the cuvette and a tunable particle rate from $5 \times 10^4\ \text{s}^{-1}$ to about $4.5 \times 10^7\ \text{s}^{-1}$ with an entrance energy of 8.3 MeV. Accelerated alpha particles pass through an exit window (1 mm diameter) fitted with a foil stack consisting of a $10\ \mu\text{m}$ thick scintillator (for online rate monitoring), a $3\ \mu\text{m}$ thick Al foil and a $5\ \mu\text{m}$ thick Mylar foil, sealing the high vacuum of the beam tube to the atmospheric air. Then, after a short air gap of 1 mm to 2 mm, the ion beam enters a 100 mm long cylindrical cuvette through a thin entrance window made of Mylar, $1.2\ \mu\text{m}$ thick. The cuvette is made of synthetic quartz with good optical transparency (transmission above 90%) in the wavelength range from 200 nm to 2500 nm (Hellma Analytics). The cuvette is filled and permanently flushed at predefined flow rates of up to $5\ \text{L}\cdot\text{min}^{-1}$ with selected gases at atmospheric pressure, using a gas mixing and supply system based on mass flow controllers [see Fig. 4(a)]. Alpha particles with energies below 8.3 MeV were generated by inserting Al foils with a thickness of less than $26\ \mu\text{m}$ as an energy attenuator in the air gap between the beam exit window and the quartz cuvette.

The radioluminescence mapping capability of the developed radioluminescence detection systems was tested with (a) accelerated alpha particles at the PIAF [see Fig. 4(a)], (b) an extended Am-241 source having an activity of 980 kBq [see Fig. 4(b)], and (c) with five groups of pitchblende minerals, with each group having an activity up to 1.5 kBq, see Fig. 4(c) [29]. In Fig. 4(b), the Am-241 active layer of $20\ \text{mm} \times 100\ \text{mm}$ is fixed in an Ag-foil with a thickness of 0.25 mm. The radionuclide layer is covered by a $2\ \mu\text{m}$ pure Au layer. The source is housed inside an evacuable gas vessel with a quartz dome. This allows the space around the source to be filled with selected gases and the radioluminescence outside the chamber to be studied in the entire relevant wavelength range above 230 nm. In all cases, the optical detection systems were set up at a distance of 2 m from the source, see Fig. 5.

For all measurements in the UV-C spectral region, the Hamamatsu PMT with CsTe photocathode (H11870-09) was used with bandpass interference filters having a bandwidth of 16 nm and center wavelength of 260 nm (FF01-260/16-25, Semrock Inc.). In the UV-A spectral range, Hamamatsu PMT with ultra-bialkali photocathode (H10682-210) was used with interference filters centered at 337 nm with a bandwidth of 10 nm (# 65-128, Edmund Optics). Both PMTs were selected for a very low dark rate, i.e. the UV-C PMT has a dark count rate of less than $1\ \text{s}^{-1}$, while the UV-A has less than $10\ \text{s}^{-1}$.

4. Experimental results and discussion

Fig. 6 shows the radioluminescence count rate measured at PIAF as a function of alpha particle rate. The cuvette where alpha particles were stopped was filled with air at atmospheric pressure. All lens systems were positioned 2 m from the cuvette and oriented so that the location where the alpha particle energy loss is greatest (the Bragg peak) was on the optical axis. With a field of view larger than the range of alpha particles in air ($\sim 38\ \text{mm}$), they capture about the same radioluminescence light as if it would be emitted from a point alpha source. In this context, rates in particles per second will be expressed hereafter in becquerels (Bq), which is a more practical unit to explain the performance of optical detection systems. With the UVFS and the Fresnel 1 ($D_1 = 452.9\ \text{mm}$) lens system radioluminescence was measured in the UV-C, while with Fresnel 2 ($D_2 = 257.6\ \text{mm}$) lens system operated in the UV-A spectral region. Having a similar f-number, the results of Fresnel 1 lens system can be mapped into Fresnel 2 system using the factor $(D_2/D_1)^2$, and vice versa. The background count rate with room lighting switched off, but surrounding control lights of electronics and monitors still on,

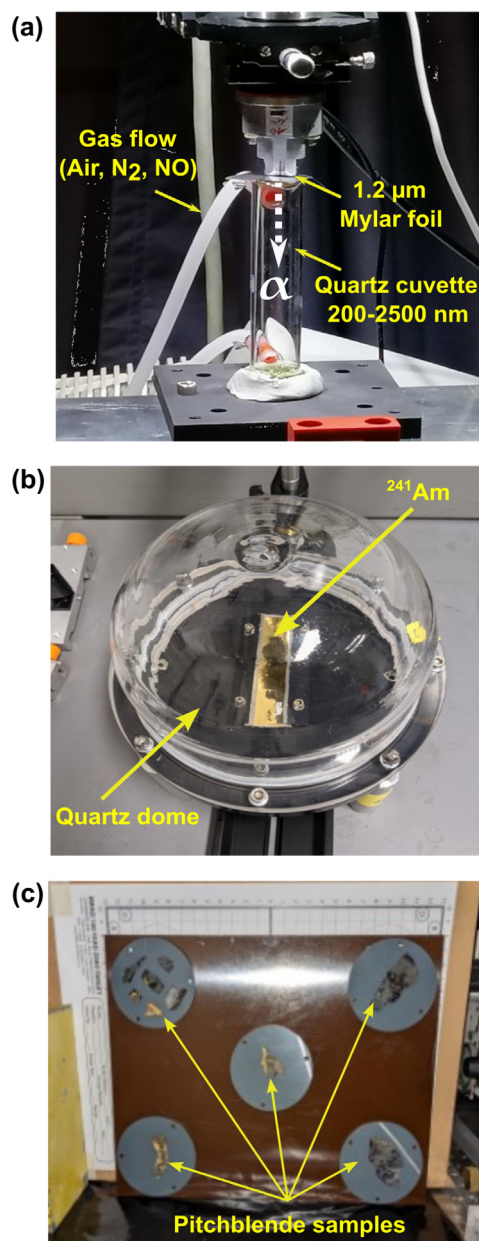


Fig. 4. (a) Photo of the alpha particle interaction region at the PIAF. The PIAF microbeam was focused into a quartz cuvette (Hellma Analytics, cylindrical quartz cuvette with two tubes, wavelength range 200 nm–2500 nm, 100 mm path length) which could be filled with different gases (air, N_2 , N_2+NO mixture). (b) Photograph of the Am-241 source (Eckert & Ziegler Cesio) inside a quartz dome. (c) Arrangement of pitchblende mineral samples. The samples were cut from pitchblende-bearing ores with a micro water jet into slices with flat unpolished surface (for details, see [29]).

was around $1\ \text{s}^{-1}$ in the UV-C and $600\ \text{s}^{-1}$ in the UV-A. With the light in the accelerator hall switched on, the background count rate was about $3\ \text{s}^{-1}$ in the UV-C and $2 \times 10^6\ \text{s}^{-1}$ in the UV-A.

In all cases, the radioluminescence count rate is linearly proportional to the alpha particle rate. At a reference distance of 2 m between the radioluminescence source (i.e., the cuvette in which the alpha particles are stopped) and the receiving optics, both lens systems capture a part of the alpha particle path length around the Bragg peak (i.e., the last 3 cm of their path). Since the energy loss curves around the Bragg peak are similar for energies between 5 MeV and 8.3 MeV used in these experiments, the sensitivity of both systems is relatively independent of the alpha particle energy. This observation can be seen in Fig. 6, where the radioluminescence count rates measured with

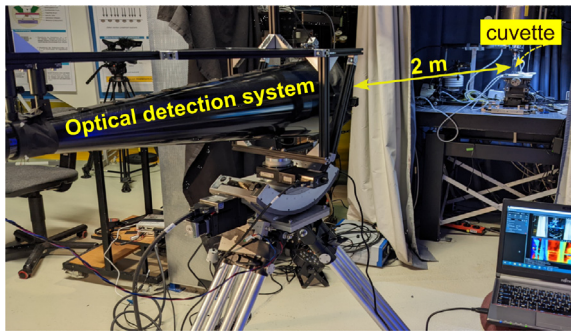


Fig. 5. Photograph of the experimental setup at the PIAF. All optical detection systems were positioned 2 m away from the alpha particle source. In imaging mode, the UVFS system mounted on two motorized stages (Newport goniometer M-BGM160PE and rotation stage RVS80CC) was scanning the area around the alpha source.

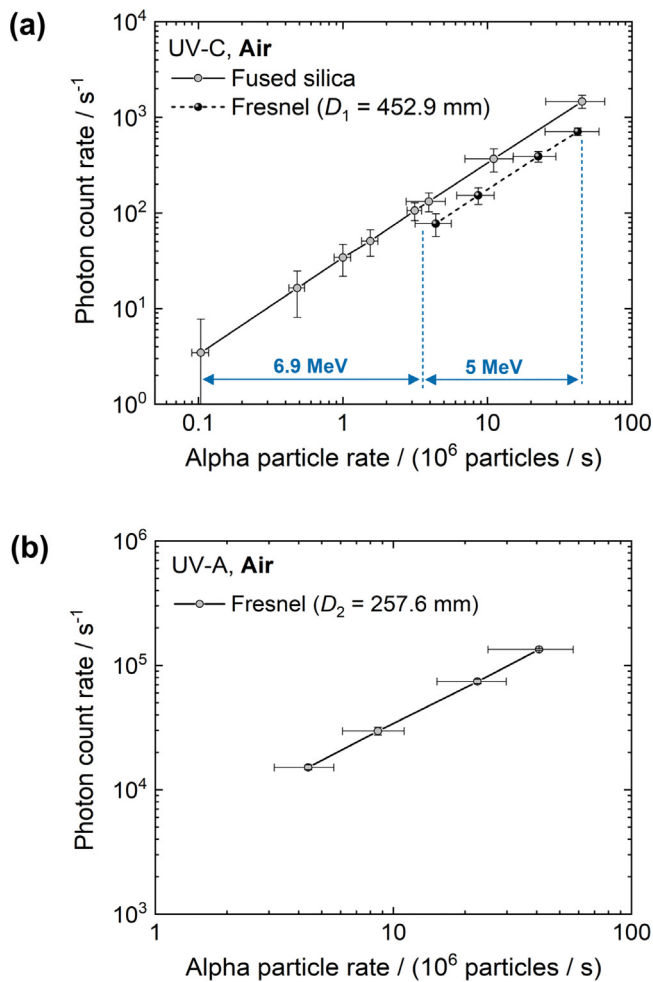


Fig. 6. (a) Comparison of UV-C radioluminescence sensitivities in air measured at the PIAF at a reference distance of 2 m between the radioluminescence source and lens. The slopes of linear fits are $34(6)\text{s}^{-1}\text{MBq}^{-1}$ for the UVFS and $17(3)\text{s}^{-1}\text{MBq}^{-1}$ for the Fresnel 1 ($D_1 = 452.9\text{ mm}$) lens systems at a background rate of $0.7(27)\text{s}^{-1}\text{MBq}^{-1}$ for both systems. Due to the finite FOV of both systems, the sensitivities for alpha particle energies of 5 MeV and 6.9 MeV are similar. (b) UV-A radioluminescence count rate generated by 5 MeV, measured with the Fresnel 2 lens system ($D_2 = 257.6\text{ mm}$). The signal slope is $3400(500)\text{s}^{-1}\text{MBq}^{-1}$.

alpha particles having energies 5 MeV and 6.9 MeV fall into the same slope. Uncertainties reported in text and figures correspond to standard deviations given with a 95% confidence interval ($k = 2$). In air, an ISO 11929-4 [30] detection limit as low as 270 kBq could be achieved

with the UVFS system at a distance of 2 m using 1 s PMT integration time. The Fresnel lens system, on the other hand, is less sensitive (about a factor of 2) in the UV-C spectral range due to the transmission limit at 260 nm, but very efficient in the UV-A spectral range due to its high transmission and large geometric efficiency (see Fig. 1). The large uncertainty of microbeam alpha rate comes from instability of the beam monitoring apparatus. The systematic uncertainties for the alpha-particle count rate are larger and not that well defined. The online count rate monitor, based on a 10 μm scintillator foil and a small PMT, had been designed for minimum degrading of the microbeam and for low count rates. For the present high count rates a fast pulse processing system with reduced noise discrimination had to be used, which was frequently calibrated against a Si particle detector in place of the cuvette. Another source of uncertainty was increasing pulse pileup at the high count rates above about $1 \times 10^6\text{ s}^{-1}$. The alpha particles arrive in bunches corresponding to the cyclotron frequency of 8.94 MHz. The pileup fractions were measured at several high rates, compared to calculations and corrections of the online monitor count rate were applied. In addition, the very high rates around $1 \times 10^7\text{ s}^{-1}$ for extended periods could have led to degradation of the thin foils and loss of counting efficiency. During the later experiments the beam was defocused, and the scintillator foils were exchanged several times. The systematic uncertainties of the alpha particle count rate are estimated at about 10% (at $k = 2$).

In the UV-A spectral region, the sensitivity of the Fresnel lens system ($D_2 = 257.6\text{ mm}$) is $3400(500)\text{ s}^{-1}\text{MBq}^{-1}$. At a background count rate of 600 s^{-1} , this sensitivity allows a detection limit of 35 kBq using 1 s PMT integration time. A similar detection sensitivity holds also for the UVFS lens system. Both systems can achieve a detection limit of about 4 kBq in a background-free environment (e.g., in darkened rooms or, in some cases, during a nighttime operation).

The measured sensitivities in the UV-C and UV-A spectral regions compare well with those calculated assuming a source fully immersed in the field of view of the optical detection system (source size + alpha range in a gas). Here, the count rate can be approximated via the integration of the radioluminescence spectrum, transmission curves of optical elements on the light path, and the PMT count sensitivity curve. The counting efficiency s of the detector (count rate per activity) can be expressed as an integral of the following form [5,6]:

$$s = \frac{\Omega}{4\pi} \cdot \int Y(\lambda) \cdot T_{\text{src}}(\lambda) \cdot T_{\text{lens}}(\lambda) \cdot T_{\text{filt}}(\lambda) \cdot QE(\lambda) \cdot d\lambda \quad (1)$$

where Ω is the solid angle in steradians, $Y(\lambda)$ photon yield expressed in photons per alpha particle [5], $T_{\text{src}}(\lambda)$ is the transmission of the source enclosure (quartz cuvette for the beam), $T_{\text{lens}}(\lambda)$ is the lens transmission, $T_{\text{filt}}(\lambda)$ is the filter assembly transmission, and $QE(\lambda)$ is the quantum efficiency of the PMT in counts per photon. Filter transmission and quantum efficiencies of PMTs can be found on the manufacturers' websites (see Table 1). The contribution of absorption of ultraviolet photons in air separating the source and the detector, deviations from dry air STP conditions, the angle of incidence on a filter and lens edges are negligible and therefore have been neglected. The comparison between the calculated and the measured sensitivities for the three detector systems (cf. Fig. 3) in four configurations is shown in Table 1. From Table 1 it is evident that Eq. (1) yields slightly higher numbers than measured but still very reasonable. It can be seen that the ratio of UV-C sensitivities between UVFS and Fresnel systems is remarkably well reproduced; the absolute UV-C values are well within the uncertainty range. The estimated UV-A sensitivity is 25% higher than measured, probably due to a field of view not fully covering the extent of radioluminescence emitting volume; also, UV-A PMT window is much smaller than that of UV-C which significantly complicates the alignment, thus bringing forth various edge effects.

The radioluminescence signal in the UV-C spectral region can be enhanced significantly by purging the space around the alpha source with N_2+NO gas mixture [9–11,15]. With the optical detection setups presented in this work, a signal enhancement up to four orders

Table 1

Comparison between calculated sensitivities using Eq. (1) and those measured with the three lens-based radioluminescence detection systems.

Detection system	Lens material	Filters	PMT	Calculated sensitivity ($s^{-1} MBq^{-1}$)	Measured sensitivity ($s^{-1} MBq^{-1}$)
UVFS in UV-C	UV fused silica	2 filters (FF01-260/16–25, Semrock Inc.)	Hamamtsu H11870-09	36	34 ± 6
UVFS in UV-A	UV fused silica	2 filters (65–128, Edmund Optics)	Hamamtsu H10682-210	3810	Not measured
Fresnel 1 in UV-C	PMMA	2 filters (FF01-260/16–25, Semrock Inc.)	Hamamtsu H11870-09	18	17 ± 3
Fresnel 2 in UV-A	PMMA	2 filters (65–128, Edmund Optics)	Hamamtsu H10682-210	4500	3400 ± 500

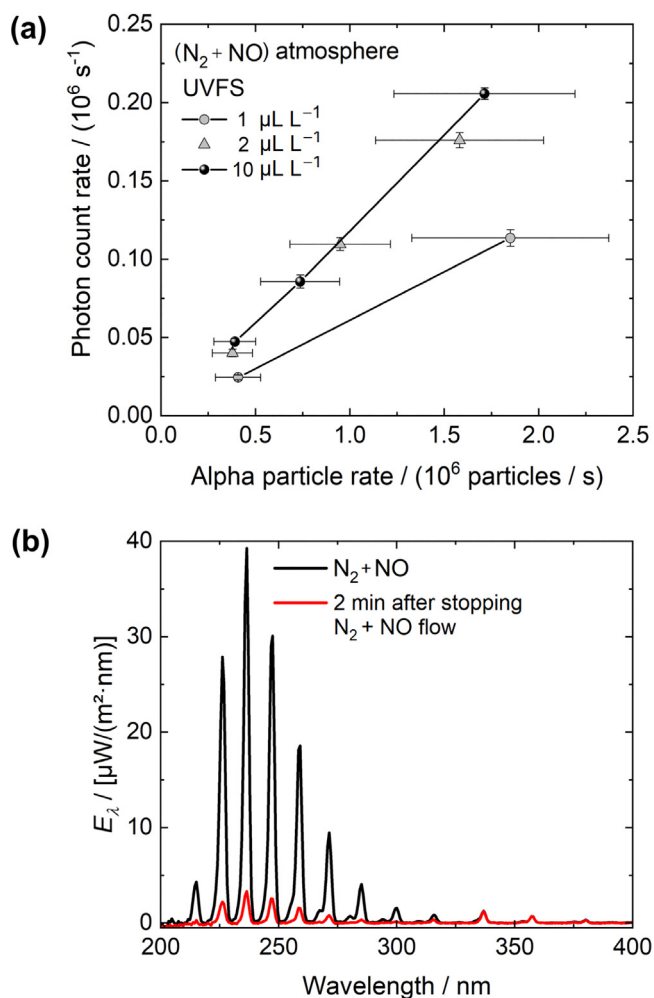


Fig. 7. (a) UV-C radioluminescence count rate generated by 5 MeV alpha particles, measured at the PIAF at a reference distance of 2 m between the radioluminescence source and the UVFS lens. The UV-C counting rate can be increased by more than three orders of magnitude by purging the cuvette with a $N_2 + NO$ gas mixture at a NO concentration above $2 \mu L L^{-1}$. The UV-C sensitivity at $2 \mu L L^{-1}$ is $1.3 \times 10^5 s^{-1} MBq^{-1}$. At NO concentrations above $2 \mu L L^{-1}$, the UV-C signal saturates. A similar trend is observed also with the Fresnel lens system. (b) Radioluminescence emission spectrum of NO measured at the PIAF at a nominal alpha particle rate of about $30 \times 10^6 s^{-1}$ with a PTB-calibrated array spectroradiometer. Two minutes after stopping the flow of NO and N_2 , the UV-C radioluminescence signal drops by a factor of 10 relative to the one measured with $N_2 + NO$ purging.

of magnitude relative to the signal measured in the air atmosphere could be measured. Fig. 7 shows the dependence of the UV-C count

rate measured with the UVFS lens system as a function of the alpha particle rate at three NO concentrations. These data indicate that the radioluminescence signal has a linear dependence on the alpha particle rate and the signal increase goes into saturation at a NO concentration of $2 \mu L L^{-1}$. At NO concentrations between $2 \mu L L^{-1}$ and $10 \mu L L^{-1}$ used in this work, detection limits [30] as low as 100 Bq with room lighting on, and 70 Bq in a dark environment could be achieved, using a PMT integration time of just 1 s.

The increase of the signal in the $N_2 + NO$ mixture is due to excitation transfer from N_2 to NO [9,10]. In this process, molecular nitrogen in the long-lived $N_2 A^3 \Sigma_u^+$ state collides with NO molecules and excites ground state nitric oxide to the $NO A^2 \Sigma^+$ state, while the N_2 molecule loses its excitation and decays to the ground state. Therefore, this signal amplification is associated with the excited NO molecules which emit in the UV-C. The radioluminescence in the UV-A spectral region from the fast-decaying higher level $N_2 C$ -states is not affected by this process.

This signal amplification, combined with the high sensitivity of the detection systems developed in this work, can greatly facilitate the management of radiological emergencies, especially in confined spaces where it is feasible to flood a contaminated area with a suitable $N_2 + NO$ mixture and quickly detect UV-C radioluminescence to locate the sources of alpha radiation while keeping personnel at a safe distance. This approach can also help inspect various installations during decommissioning of old nuclear plants. However, in the environment, leveraging the benefits of $N_2 + NO$ enhancement could be more problematic, depending on conditions such as wind and precipitation. Part of the difficulty in using this approach for contamination mapping lies in the rapid quenching of the $N_2 A^3 \Sigma_u^+$ states and thereby the UV-C radioluminescence from NO by atmospheric gases such as O_2 and H_2O . Due to the slow process of collisional energy transfer from the excited N_2 to the NO molecules even very small amounts of O_2 or water are enough to remove a substantial amount of the stored energy in the populated A-states of N_2 before they have a chance to transfer this energy to NO and decay there via UV-C emission [9,10]. Fig. 7(b) shows the sensitivity of NO radioluminescence after stopping $N_2 + NO$ gas flow. From the data it is evident that just 2 min after the stop of N_2 and NO gas flow, the UV-C radioluminescence intensity is decreased by more than a factor of 10. Therefore, a highly sensitive detection system that can measure a significant amount of UV-C radioluminescence within few seconds is required to exploit the full potential of NO radioluminescence enhancement in the UV-C spectral region.

Radioluminescence mapping of an contaminated area is an important feature for emergency managements. This allows imaging of contaminations with alpha-emitting radionuclides from a distance, without exposing personnel and devices to the radiation itself. In this imaging approach, the UV-C radioluminescence image is superimposed on the conventional image obtained under normal lighting. The conventional image provides coordinates for the contamination and the UV-C image contains quantitative information on the activity of the alpha emitter, since the intensity of radioluminescence is proportional to the total

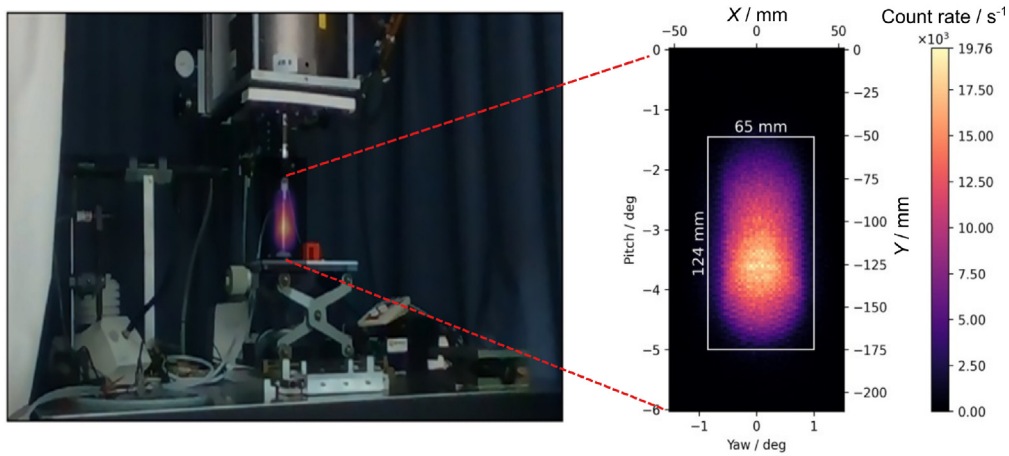


Fig. 8. UV-C radioluminescence image of 8.3 MeV alpha particles exiting the PIAF and stopping in the nitrogen filled quartz cuvette. This image is shown for illustrative purposes to demonstrate the mapping capability of the UVFS lens system shown in Fig. 3(a) and has been measured at an alpha particle rate higher than $5 \times 10^7 \text{ s}^{-1}$, which is above the counting capacity of the online mirobeam monitoring system. The area around the quartz cuvette where the accelerated alpha particles were stopped has been scanned with the UVFS system from a distance of 2 m. The radioluminescence image has been superimposed on a conventional photograph, with the coordinates of both images correlated by ray tracing.

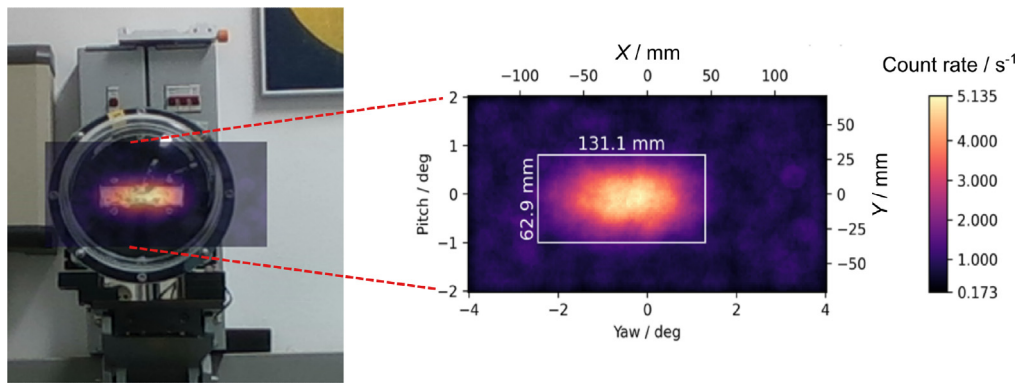


Fig. 9. UV-C radioluminescence image of the ^{241}Am source [cf. Fig. 4(b)]. The radioluminescence image has been obtained by scanning the area around the sample with the UVFS system from a distance of 2 m with a 2 s counting time per scan pixel. The radioluminescence image has been superimposed on a conventional photograph, with the coordinates of both images correlated by ray tracing.

energy loss of alpha particles in the air. The imaging capability of the UVFS lens system is demonstrated in Figs. 8, 9 and 10. A typical UV-C radioluminescence mapping of alpha particles stopped in the cuvette is shown in Fig. 8. The left panel shows the UV-C radioluminescence image superimposed on a conventional photograph, with the coordinates of both images correlated by ray tracing. The 2D distribution of the UV-C radioluminescence signal with a 1 s PMT integration time per pixel is shown in the right panel. Radioluminescence light emission occurs around the alpha source in a volume whose extent is approximately equal to the range of alpha particles measured in air (76.7 mm for 8.3 MeV alpha particles). As the FOV of the detection system at the object plane is about 50 mm, the overlapping of adjacent scanning points caused some image blurring. The radioluminescence image was smoothed by convolving the original image with the uniform circular kernel of 10 mm in diameter. The background of the image computed from all pixels outside the drawn box is about 50 s^{-1} , while the highest signal is about $2 \times 10^4 \text{ s}^{-1}$.

Radioluminescence mapping of an extended ^{241}Am source [cf. Fig. 4(b)] of measured activity of 980 kBq in air atmosphere is demonstrated in Fig. 9. Same as in Fig. 8, the UV-C image is superimposed onto the conventional image to provide the spatial coordinates of the alpha emitting active area. The counting time per scanning point was 2 s, with a background count rate of $0.8(4) \text{ s}^{-1}$ and a maximum count rate of 5.1 s^{-1} .

Fig. 10 shows radioluminescence imaging of low activity pitchblende minerals in air, taken with the UVFS lens system at a

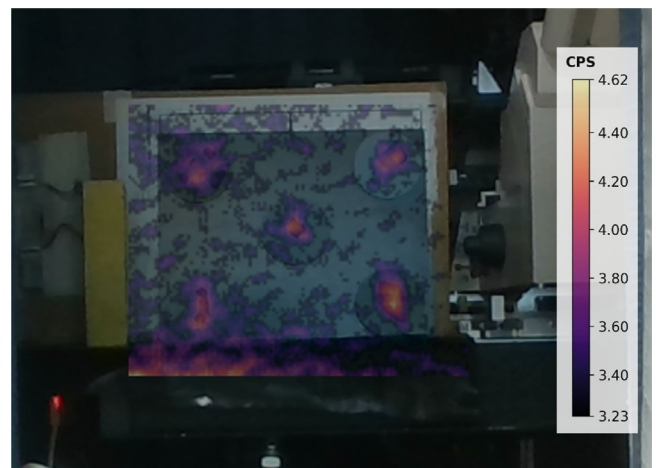


Fig. 10. UV-A radioluminescence image of the pitchblende mineral samples shown in Fig. 4(c) overlaid with the conventional image. The image has been obtained by scanning the area around the source panel with a UVFS system from 2 m.

source-to-detector distance of 2 m. Each sample group has a detectable alpha count rate between 1 kBq and 1.5 kBq or a surface activity between 80 Bq cm^{-2} and 105 Bq cm^{-2} measured by alpha-track-detection

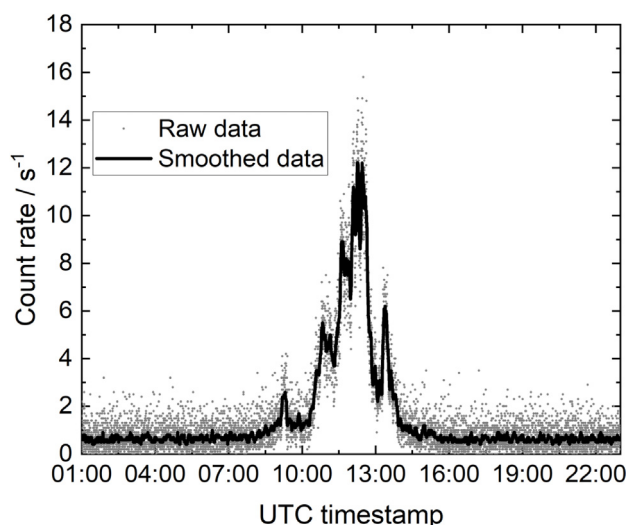


Fig. 11. Ambient background light measured by the UVFS lens system. The filtering setup consists of a stack of 2 UV-C filters (FF01-260/16-25, Semrock Inc.) coupled to a CsTe photocathode PMT (H11870-09, Hamamatsu). Similar values hold also for the Fresnel lens system.

and alpha-spectroscopy (grid ionization chamber). Characterization of pitchblende samples using various techniques such as alpha track, grid ionization chamber, and radioluminescence has been reported in a separate paper [29]. Since the radioluminescence yield in air in the UV-C spectral region (100 nm to 280 nm) is about 200 times lower than in the UV-A and UV-B regions, these low activity samples could only be imaged in the UV-A spectral region. With a counting time per pixel of 20 s, a maximum signal count rate of 4.6 s^{-1} was obtained with a background signal of $3.17(24) \text{ s}^{-1}$. Some reflections from different background lights in the room interfered with the lower part of the scan but did not affect the localization of the samples.

In the daylight, specifically outdoors, the background ambient light can significantly lower the activity these systems can detect. However, careful matching of the diameter and focal length of the receiving optics, the response of the photocathode, and the passband of the filter in conjunction with light-tight covering of all sensitive parts can mitigate the effects of the background ambient light considerably. Fig. 11 demonstrate the ambient background light with the UVFS lens system pointing towards the window in a conventional office. When the Sun sets in the horizon, a background count rate of 16 s^{-1} is expected. During the rest of the time, the background signal is relatively low (about 1 s^{-1}), slightly lower than that in the PIAF accelerator hall with the fluorescent lights on (about 3 s^{-1}).

5. Conclusion

Laboratory tests have demonstrated that lens systems with large diameter and long focal length enhance the detection limit while keeping the background signal low. In the air, the UV-C sensitivity at 2 m detection distance is $34(6) \text{ s}^{-1} \text{ MBq}^{-1}$ for the UVFS and $17(3) \text{ s}^{-1} \text{ MBq}^{-1}$ for the large diameter ($D_1 = 452.9 \text{ mm}$) Fresnel lens system. The sensitivity is expressed in terms of the count rate per activity measured by the detection system in its field of view while the detection limits are expressed in terms of the measured activity. In the air, therefore, an ISO 11929-4 [30] detection limit of 270 kBq could be achieved with the UVFS lens system and 540 kBq with a Fresnel lens system using 1 s PMT integration time. For samples with thick deposition layer, the self-absorption of the material impairs the detection limit. The impact depends on the thickness and density of the layer. The results reported in the paper, however, refer to the measured activities rather than the activity in the bulk material. The Fresnel lens system is less sensitive

(about a factor of 2) in the UV-C spectral range due to the transmission limit at 260 nm, but very efficient in the UV-A spectral range due to its high transmission and large geometric efficiency. In UV-A, a detection limit of 4 kBq is achieved with the UVFS system at 1 s PMT integration time, and about 1.4 kBq is expected with the large diameter Fresnel lens system. Being lightweight, the Fresnel lens system can be easily integrated in a UAV with moderate payloads (less than 5 kg).

The measured sensitivities in the UV-C and UV-A spectral regions compare well with those calculated assuming a source fully immersed in the field of view of the optical detection system, with a radioluminescence photon yield inferred from the spectra measured in Ref. [5]. While in the UV-C region the agreement between the simulated and calculated sensitivities is within the uncertainty limits, the calculated sensitivity in the UV-A region is 25% higher than the measured sensitivity due to field-of-view effects related to the smaller UV-A PMT window.

The detection limit in the UV-C can be enhanced up to about four orders of magnitude by applying a $\text{N}_2 + \text{NO}$ purge. This allows detection limits of as low as 70 Bq. Since ambient oxygen and water vapor significantly attenuate the UV-C radioluminescence signal, purging with an optimal mixture of NO and N_2 in conjunction with a fast detection system is critical for the successful detection of low activity samples. The presence of ambient UV background light, whether from sunlight or artificial sources, remains an important factor affecting detection limits and needs to be further optimized both technically and through data processing methods.

By combining these optical detection systems with automatic scanning of the contaminated area and the wireless data collection and transmission technology, one overcomes all drawbacks of the conventional alpha detection techniques by keeping both the operator and the equipment out of the danger zone and providing real-time information on the source location and morphology, facilitating the onsite incident management, evacuation plans as well as in developing strategies for protecting the public from harm [20].

Declaration of competing interest

The authors declare that they have no known competing financial interests or personal relationships that could have appeared to influence the work reported in this paper.

Data availability

Data will be made available on request.

Acknowledgments

The project 19ENV02 RemoteALPHA has received funding from the EMPIR programme co-financed by the Participating States and from the European Union's Horizon 2020 research and innovation programme. 19ENV02 RemoteALPHA denotes the EMPIR project reference. F. S. K. and V. D. would like to thank I. Kröger (PTB) and P. Sperfeld (PTB) for providing the PTB-calibrated array spectroradiometer and support in the evaluation of the radioluminescence spectra. The authors would like to thank also O. Döhr, T. Heldt, E. Holland and J. Pieper for the operation of the PTB cyclotron.

References

- [1] L.A. Burchfield, *Radiation Safety: Protection and Management for Homeland Security and Emergency Response*, Wiley, 2009.
- [2] S.N. Ahmed, *Physics and Engineering of Radiation Protection*, Academic Press, 2007.
- [3] A.J. Crompton, K.A.A. Gamage, A. Jenkins, C.J. Taylor, *Alpha particle detection using alpha-induced air radioluminescence: A review and future prospects for preliminary radiological characterisation for nuclear facilities decommissioning*, *Sensors* 18 (2018) 15.

- [4] S.M. Baschenko, Remote optical detection of alpha particle sources, *J. Radiol. Prot.* 24 (2004) 75.
- [5] J. Sand, Alpha Radiation Detection via Radioluminescence of Air (Ph.D. thesis), Tampere University of Technology, Tampere, Finland, 2016, Publication; Vol. 1449.
- [6] J. Sand, S. Ihanola, K. Peräjärvi, H. Toivonen, J. Toivonen, Radioluminescence yield of alpha particles in air, *New J. Phys.* 16 (2014) 053022.
- [7] J. Sand, I. S., A. Nicholl, K. Peräjärvi, H. Toivonen, J. Toivonen, Imaging of alpha emitters in a field environment, *Nucl. Instrum. Methods Phys. Res. A* 782 (2015) 13.
- [8] J. Sand, A. Nicholl, E. Hrneck, H. Toivonen, J. Toivonen, Peräjärvi, Stand-off radioluminescence mapping of alpha emitters under bright lighting, *IEEE Trans. Nucl. Sci.* 63 (2016) 1777.
- [9] T. Kerst, J. Toivonen, Intense radioluminescence of NO/N₂-mixture in solar blind spectral region, *Opt. Express* 26 (2018) 33764.
- [10] T. Kerst, Optical Stand-Off Detection of Alpha Radiation in Nuclear Facilities (Ph.D. thesis), Tampere University, Tampere, Finland, 2019, Tampere University Dissertations 129.
- [11] T. Kerst, J. Toivonen, Dynamic enhancement of nitric oxide radioluminescence with nitrogen purge, *Sci. Rep.* 9 (2019) 13884.
- [12] T. Kerst, J. Sand, S. Ihanola, K. Peräjärvi, A. Nicholl, E. Hrneck, H. Toivonen, J. Toivonen, Standoff alpha radiation detection for hot cell imaging and crime scene investigation, *Opt. Rev.* 25 (2018) 429.
- [13] F. Lamadie, F. Delmas, C. Mahe, P. Gironès, C. Le Goaller, J.R. Costes, Remote alpha imaging in nuclear installations: New results and prospects, *IEEE Trans. Nucl. Sci.* 52 (2005) 3035.
- [14] O.P. Ivanov, V.E. Stepanov, S.V. Smirnov, V.A. G., Development of method for detection of alpha contamination with using UV-camera "DayCor" by OFIL, in: Nuclear Science Symposium and Medical Imaging Conference (NSS/MIC), IEEE, Valencia, 2011, pp. 2192–2194.
- [15] F.S. Krasniqi, T. Kerst, M. Leino, J.-T. Eiseh, H. Toivonen, A. Röttger, J. Toivonen, Imaging of alpha emitters in a field environment, *Nucl. Instrum. Methods Phys. Res. A* 987 (2021) 164821.
- [16] J. Yao, J. Brenizer, R. Hui, S. Yin, Standoff alpha radiation detection via excited state absorption of air, *Appl. Phys. Lett.* 102 (2013) 254101.
- [17] D. Kim, D. Yu, A. Sawant, M.S. Choe, I. Lee, S.G. Kim, E.M. Choi, Remote detection of radioactive material using high-power pulsed electromagnetic radiation, *Nature Commun.* 8 (2017) 15394.
- [18] P. Sprangle, B. Hafizi, H. Milchberg, G. Nusinovich, A. Zigler, Active remote detection of radioactivity based on electromagnetic signatures, *Phys. Plasmas* 21 (2014) 013103.
- [19] K. Konthasinghe, K. Fitzmorris, M. Peiris, A.J. Hopkins, B. Petrak, D.K. Killinger, A. Muller, Laser-induced fluorescence from N₂⁺ ions generated by a corona discharge in ambient air, *Appl. Spectrosc.* 69 (2015) 1042.
- [20] EURAMET, 19ENV02 RemoteALPHA, Remote and real-time optical detection of alpha-emitting radionuclides in the environment, 2022, <https://www.euramet.org/research-innovation/search-research-projects/details/project/remote-and-real-time-optical-detection-of-alpha-emitting-radionuclides-in-the-environment/>, accessed: 2022-07-28.
- [21] To be published elsewhere.
- [22] Thorlabs, Uncoated UVFS transmission, 2022, https://www.thorlabs.com/newgrouppage9.cfm?objectgroup_id=3983, accessed: 2022-07-28.
- [23] PMMA transmission curves provided by the manufacturer Orafol Fresnel Optics.
- [24] Hamamatsu, Photon counting head H11870-09 datasheet, 2022, https://www.hamamatsu.com/content/dam/hamamatsu-photronics/sites/documents/99_SALES_LIBRARY/etd/H11870_TPMO1061E.pdf, accessed: 2022-07-28.
- [25] Hamamatsu, Photon counting head H10682-210 datasheet, 2022, https://www.hamamatsu.com/content/dam/hamamatsu-photronics/sites/documents/99_SALES_LIBRARY/etd/H10682_TPMO1075E.pdf, accessed: 2022-07-28.
- [26] Semrock, FF01-260/16-25 transmission, 2022, <https://www.semrock.com/filters.aspx>, accessed: 2022-07-28.
- [27] Edmund Optics, 337nm hard coated bandpass interference filter, 10nm FWHM bandwidth, 2022, <https://www.edmundoptics.de/p/337nm-cwl-25mm-dia-hard-coated-od-4-10nm-bandpass-filter/19781/>, accessed: 2022-07-28.
- [28] K.D. Greif, H.J. Brede, D. Frankenberg, U. Giesen, The PTB single ion microbeam for irradiation of living cells, *Nucl. Instrum. Methods Phys. Res. B* 217 (2004) 505.
- [29] A. Klose, M. Luchkov, V. Dangendorf, A. Lehnert, C. Walther, On the way to remote sensing of alpha radiation: radioluminescence of pitchblende samples, *J. Radioanal. Nucl. Chem.* (2022) <https://doi.org/10.1007/s10967-022-08540-6>.
- [30] ISO 11929-4, Determination of the Characteristic Limits (Decision Threshold, Detection Limit and Limits of the Coverage Interval) for Measurements of Ionizing Radiation-Fundamentals and Application-Part 4: Guidelines to Applications, pub-ISO, 2018.